COMMUNICATION

An Unprecedented π-Electronic Circuit Involving an Odd Number of Carbon Atoms in a Grossly Warped Non-Planar Nanographene

Received 00th January 20xx,
Accepted 00th January 20xx

DOI: 10.1039/x0xx00000x

Sílvia Escayola,[a,b] Albert Poater,[a] Alvaro Muñoz-Castro*[c] and Miquel Solà*[a]

The formation of π-aromatic circuits along a grossly warped nanographene, $C_{80}H_{30}$, containing five- and seven-membered rings inserted into a six-membered mesh, reveals global π-circuits at the edge of the backbone. Based on DFT calculations, one of the two most favorable circuits for π-electron delocalization has formally 50 π-electrons abiding Hückel's rule, whereas, the second one formally has 75 π-electrons and, remarkably, it does not follow any of the known rules of aromaticity.

Since the early rationalization of benzene bonding structure depicted by Kekule´s seminal work more than one and half-century ago,[1–3] aromatic molecules have arisen the interest of the scientific community.[4–12] Fused ring species, such as polycyclic aromatic hydrocarbons (PAHs), fullerenes, and porphyrins, to name a few, are challenging cases owing to the presence of different aromatic or antiaromatic circuits of local or global character.[13–21]

The incorporation of extended fused rings in a PAH structure following the continuous development of synthetic strategies[22–24] allows further exploration of the chemistry of finite nanographenes with promising shapes, properties, and applications. The hexagonal honeycomb-like arrangements found in benzenoid PAH lead to planar geometries. Defects in the form of non-hexagonal rings in such networks cause distortions away from planarity. Non-planar π-extended PAHs can be achieved with the presence of five- or seven-membered rings in the structural backbone,[25] resulting in a curved surface to release the strain given by the incorporation of different ring sizes in a hexagonal mesh. In this sense, pentagons induce a positive curvature of the surface, as observed in corannulene with a characteristic bowl-shape,[26] whereas heptagons induce a negative curvature, as denoted in [7]circulene with a saddle-shaped surface.[27,28]

The grossly warped nanographene ($C_{80}H_{30}$, **1**), which was synthesized by Itami and Scott in 2013,[29] exploits the presence of both bowl- and saddle-shaped sections in a 26-ring nanographene proving the consequences of multiple odd defects in the π-extended PAH. This nanographene (**1**) obtained by successive expansion of corannulene ($C_{20}H_{10}$)[29] contains a central pentagon and five peripheral heptagons with a novel π-landscape with enhanced solubility and electronic-related properties. Like corannulene,[30,31] this grossly warped nanographene is prone to undergo a bowl-to-bowl inversion.

Whereas the aromaticity of benzenoid PAHs is usually well-described by Clar's π-sextet model,[32,33] the aromaticity of benzenoid PAHs containing defects in the form of 5- and 7-MRs is much less explored. In this work, we report our findings using density functional theory (DFT) calculations to unravel the electron delocalization characteristics of nanographene **1**. We performed energy optimizations with the BP86-D3/TZ2P method and we used the geometries obtained to carry out NMR calculations at the OPBE/TZ2P level and electron delocalization studies at the CAM-B3LYP/6-311G(d,p) level (full computational details are given in the ESI). π-Aromatic circuits are scrutinized by the electron density of delocalized bonds (EDDB),[34,35] gauge-including magnetically induced currents (GIMIC),[36–38] and induced magnetic field[39,40] calculations, besides of structural features to get insight into how aromaticity is accommodated in a highly curved and strained sp^2-surface. We aim to evaluate whether the presence of different ring-sizes in a nanographene sheet and the resulting curvature decreases or retains the aromatic properties inherent to the presence of local and global (anti)aromatic motifs along the curved π-surface. In addition, ^{13}C-NMR patterns (*fingerprint*) are studied to relate the position of the C atoms at the nanographene sheet with the different shielding/deshielding areas.

The characterized structure for $C_{80}H_{30}$ nanographene (**1**), is based on corannulene, $C_{20}H_{10}$, as a minimal isolated-pentagon-motif[41] providing a central bowl-shaped section, introducing the first curvature to the nanographene π-surface (Figure 1). The resulting depth at the central section amounts to 0.37 Å,[29] calculated at 0.44 Å in the gas phase, suggesting that the intermolecular aggregation influence the bowl-depth. The

[a] *Institute of Computational Chemistry and Catalysis and Department of Chemistry, University of Girona, C/ M. Aurèlia Capmany, 69, 17003 Girona, Spain. E-mail: miquel.sola@udg.edu*
[b] *Donostia International Physics Center (DIPC), Donostia, Euskadi, Spain.*
[c] *Grupo de Química Inorgánica y Materiales Moleculares, Facultad de Ingeniería, Universidad Autónoma de Chile, El Llano Subercaseaux 2801, Santiago, Chile. E-mail: alvaro.munoz@uautonoma.cl*

† Footnotes relating to the title and/or authors should appear here.
Electronic Supplementary Information (ESI) available: [Benchmark for aromaticity indexes and magnetic induced field for the planar counterpart. See DOI: 10.1039/x0xx00000x

bowl-inversion barrier is estimated by the authors to be 18.9 kcal·mol^{-1}, 7.4 kcal mol^{-1} larger than that of $C_{20}H_{10}$,[42] owing to the presence of the surrounding heptagons. The resulting warped structure exhibits five chiral seven-membered rings (7-MRs), denoted as *P* and *M*, resulting in two isomers, namely, *PMPMP*- and *MPMPM*-, the former being the one employed in the current work.

The ^{13}C-NMR analysis[29] provides seven peaks at 139.2, 133.8, 131.7, 129.7, 128.1, 127.5, and 122.5 ppm, as slight wide signals. The calculated values exhibit several peaks (Figure 1) accounting for the different carbon atom types owing to the fact that the relaxed structure does not possess a five-fold rotation axis, resulting in a differentiation within carbon of the same type given the variable curvature along the π-surface. More strained carbon atoms around the heptagonal rings appear at lower-field in comparison to the central section. The terminal carbons, C-H, are located at higher-field, similarly to corannulene.[43] The planar nanographene with a five-fold axis shows the "hub" and "rim" atoms from the central corannulene motif in $C_{80}H_{30}$ to be located at lower-field (162.5 and 159.4 ppm, respectively), suggesting a more strained region within such structure.

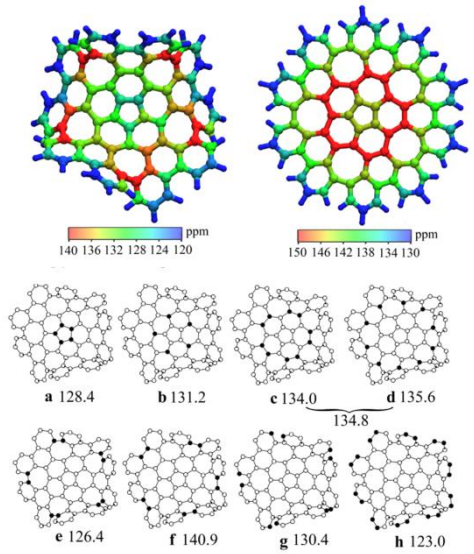

Figure 1. Calculated ^{13}C-NMR chemical shifts for warped nanographene (**1**) (above-left) and planar (above-right), and averaged calculated ^{13}C-NMR chemical shifts for warped nanographene (**1**), bottom.

Further analysis of the calculated ^{13}C-NMR values shows that the average of the similar carbon atom types agrees well with the experimentally characterized values, denoting signals at 128.4 ppm (Exp: 127.5 ppm) for the central pentagon (**a**) and 131.2 ppm for the "hub" atoms (Exp: 131.7 ppm) (**b**). Interestingly, the experimental peak at 133.8 ppm is resolved for carbons **c** and **d** on average, denoting the constant rearrangement provided by the small transition state barrier. Lastly, the signals at 126.4, 140.9, 130.4, and 123.0, account for the peripheral atoms type **e**, **f**, **g**, and **h** (Figure 1), respectively. This allows to further explore the magnetic behavior of **1**.

Moreover, the induced magnetic field (B^{ind}) is calculated to provide characteristics of the resulting shielding or deshielding regions related to the local and global aromatic properties of the individual rings and the overall nanographene structure. B^{ind} is related to the applied field (B^{ext}) via $B_j^{ind} = -\sigma_{ij}B_j^{ext}$, where the isotropic magnetic term is $B_{iso}^{ind} = -(1/3)(\sigma_{xx}+\sigma_{yy}+\sigma_{zz})B_j^{ext}$ accounting for the in-solution molecular tumbling. The resulting isotropic term (B_{iso}^{ind}, Figure 2) suggests local aromaticity at external hexagons resulting from Clar's π-sextet patterns (see Figure S2 in the ESI) owing to the shielding regions, whereas at the central pentagon and peripheral heptagons, a deshielding region is found, signifying a local antiaromatic character, also denoted by NICS(0) calculations (see Figure S3 in the ESI). This observation is also denoted from the contour-plot representation (Figure 2c), showing a shielding region for hexagons and deshielding regions for pentagon and heptagons.

Planar aromatics feature a characteristic long-range shielding response under a perpendicular field (B_z^{ext}), complemented with a perpendicular deshielding region at the ring backbone. This is rationalized as a shielding cone property depicted for different planar aromatic rings,[9,40,44–48] which is similar above and below the π-plane, as obtained for benzene.[40,45,46] For $C_{80}H_{30}$ nanographene, the bowl-shape results in a more shielded region at the concave face, where the shielding cones from aromatic hexagons interact additively, enhancing the strength and long-range characteristics of the overall structure (Figure 2c). The localized deshielding regions at the pentagon and heptagons suggest that they remain as local antiaromatic (or non-aromatic, *vide infra*) rings, embedded into the extended shielding region enabled by the aromatic hexagons and the overall structure. The planar conformation of **1** (see Figure S4 in the ESI) enhances the shielding and deshielding regions retaining the characteristics of the induced magnetic field.

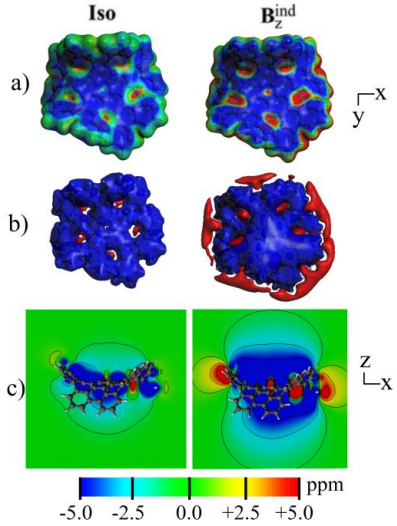

Figure 2. Induced magnetic field for warped nanographene (**1**), painted over 0.01 a.u. electron density isosurface (a), shielding and deshielding isosurface at ± 5.0 ppm (b), and as a cutplane over the *xz*-plane (c). Blue: Shielding; Red: Deshielding. See Fig. S4 for the same plots in the planar nanographene.

To further explore the presence of extended aromatic circuits along the warped nanographene, and the characteristics of each ring locally, we employed different indicators related to geometric and electronic aspects of aromaticity. We used the harmonic oscillator model of aromaticity (HOMA, values close to 1 for aromatic rings)[49] as a geometric-based indicator of aromaticity. As electronic indices we employed the fluctuation (FLU, values close to 0 for aromatic rings) and multicenter indices (MCI, see ESI), as well as the electron density of delocalized bonds (EDDB),[35,50–55] which measures the electrons delocalized through the system. In addition, the magnetic behavior of induced electronic currents along the molecular backbone is evaluated via a magnetically based index obtained from the GIMIC method.[37]

We unraveled the most favorable circuits for π-electronic delocalization in $C_{80}H_{30}$ nanographene, leading to different circuits along the nanographene as denoted in Figure 3. Interestingly, extended π-circuits involving the external hexagons are the most favorable circuits for π-electron delocalization, according to the different geometrical and electronic aromaticity indices used. The trends remain the same when going from the optimized $C_{80}H_{30}$ nanographene structure to the planar one. Despite a warped π-surface with a challenging non-planar structure, this observation indicates that non-planar nanographenes are also prone to show extended aromatic circuits. The most favorable circuits are i) the π-circuit that goes through the external rim of the most aromatic external rings (HOMA and FLU indices support this circuit as the most efficient for electronic delocalization) and ii) the same π-circuit involving the five 7-MRs (EDDB favors this circuit, see Figures S7 and S8 for EDDB plots). Note that the quantification of aromaticity by HOMA, FLU, and induced currents does not always reproduce the same trends.[56–58] The former circuit involves 50π-electrons and, therefore, follows the 4N+2 Hückel's rule with N = 12. The latter comprises 75π-electrons, an odd number of electrons, consequently not following any of the known rules of aromaticity. Indeed, the rules usually originate when counting the number of electrons that are required to reach a closed-shell structure.[59] And this is not possible with an odd number of electrons. Interestingly, the most favorable π-circuit based on the GIMIC method[37] is the latter, as can be seen in the streamline representation of the current density in the planar warped nanographene (Figure 4 and Figure S9 for the calculated net current strengths). This result is also supported by the current density plot in the plane at 2 bohr above the molecular plane of planar nanographene (see Figure S12). As can be seen, the ring current flows through the π-circuit involving the aromatic external hexagonal rings and the five 7-MRs. Additional representations of the current density plots for the planar and non-planar warped nanographene can be found in Figures S11-S13.

In conclusion, the grossly warped nanographene, $C_{80}H_{30}$, with a challenging π-landscape shows two most favorable circuits for π-electron delocalization, one with formally 50 π-electrons abiding Hückel's rule. Interestingly, the second one has formally 75 π-electrons and, therefore, it does not follow any of the known rules of aromaticity. This result represents a change of paradigm in the field of aromaticity. To our knowledge, it is the first time that an efficient π-circuit for electronic delocalization is composed by an odd number of C atoms. Further exploration of larger π-circuits in nanographenes may contribute to the understanding of extended aromatic moieties and their characteristics as the size approach to the largest aromatic species to date involving 162 π-electrons,[13] or even more extended.

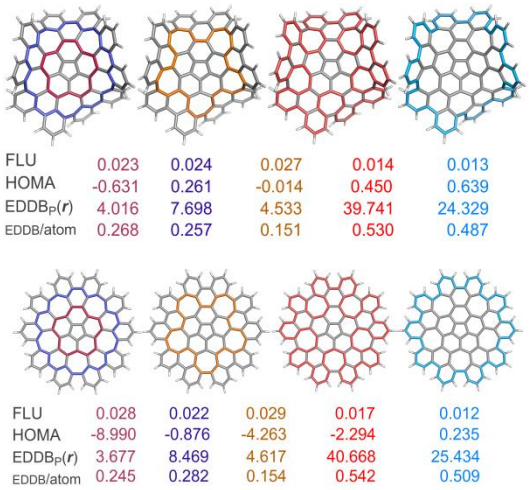

Figure 3. Aromaticity results of the selected pathways according to FLU, HOMA, and $EDDB_P(\boldsymbol{r})$ in the non-planar (above) and planar (below) *PMPMP*-enantiomer of the $C_{80}H_{30}$ nanographene.

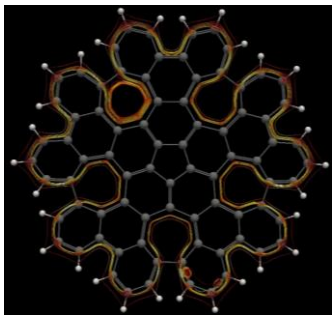

Figure 4. Streamline representation of the current density in the planar configuration of the $C_{80}H_{30}$ nanographene. The intensity of the current decreases going from white (0.1 $nA{\cdot}T^{-1}{\cdot}bohr^{-2}$), light yellow, red to black ($1{\cdot}10^{-6}$ $nA{\cdot}T^{-1}{\cdot}bohr^{-2}$). See Fig. S14 for the same representation in the non-planar *PMPMP*-enantiomer of the $C_{80}H_{30}$ nanographene.

This work was supported with funds from the Ministerio de Economía y Competitividad (MINECO) of Spain (project CTQ2017-85341-P and PGC2018-097722-B-I00) and the Generalitat de Catalunya (project 2017SGR39 and the ICREA Academia prize 2019 awarded to A.P.). S.E. thanks Universitat de Girona and DIPC for an IFUdG2019 PhD fellowship. A.P. is a Serra Húnter Fellow. A.M.-C. thanks the financial support from FONDECYT 1180683.

Conflicts of interest

There are no conflicts to declare.

References

[1] F. A. Kekulé, *Bull. la Soc. Chim. Paris* **1865**, *3*, 98–110.

[2] F. A. Kekulé, *Ann. der Chemie und Pharm.* **1866**, *137*, 129–196.

[3] A. Gero, *J. Chem. Educ.* **1954**, *31*, 201.

[4] T. M. Krygowski, H. Szatylowicz, O. A. Stasyuk, J. Dominikowska, M. Palusiak, *Chem. Rev.* **2014**, *114*, 6383–6422.

[5] T. M. Krygowski, M. K. Cyrański, *Chem. Rev.* **2001**, *101*, 1385–1420.

[6] T. Heine, C. Corminboeuf, G. Seifert, *Chem. Rev.* **2005**, *105*, 3889–3910.

[7] N. Martin, L. T. Scott, *Chem. Soc. Rev.* **2015**, *44*, 6397–6400.

[8] G. Merino, A. Vela, T. Heine, *Chem. Rev.* **2005**, *105*, 3812–3841.

[9] R. Gershoni-Poranne, A. Stanger, *Chem. Soc. Rev.* **2015**, *44*, 6597–6615.

[10] R. Papadakis, H. Ottosson, *Chem. Soc. Rev.* **2015**, *44*, 6472–6493.

[11] H. Miyoshi, S. Nobusue, A. Shimizu, Y. Tobe, *Chem. Soc. Rev.* **2015**, *44*, 6560–6577.

[12] F. Feixas, E. Matito, J. Poater, M. Solà, *Chem. Soc. Rev.* **2015**, *44*, 6434–6451.

[13] M. Rickhaus, M. Jirasek, L. Tejerina, H. Gotfredsen, M. D. Peeks, R. Haver, H.-W. Jiang, T. D. W. Claridge, H. L. Anderson, *Nat. Chem.* **2020**, *12*, 236–241.

[14] A. Muñoz-Castro, *Phys. Chem. Chem. Phys.* **2018**, *20*, 3433–3437.

[15] E. Vogel, *Angew. Chem. Int. Ed.* **2011**, *50*, 4278–4287.

[16] J. I. Wu, I. Fernández, P. v. R. Schleyer, *J. Am. Chem. Soc.* **2013**, *135*, 315–321.

[17] D. Chen, D. W. Szczepanik, J. Zhu, A. Muñoz-Castro, M. Solà, *Chem. Eur. J.* **2021**, *27*, 802–808.

[18] D. W. Szczepanik, M. Solà, T. M. Krygowski, H. Szatylowicz, M. Andrzejak, B. Pawełek, J. Dominikowska, M. Kukułka, K. Dyduch, *Phys. Chem. Chem. Phys.* **2018**, *20*, 13430–13436.

[19] R. R. Valiev, H. Fliegl, D. Sundholm, *Phys. Chem. Chem. Phys.* **2018**, *20*, 17705–17713.

[20] J. Wei, W.-X. Zhang, Z. Xi, *Chem. Sci.* **2018**, *9*, 560–568.

[21] G. Naulet, L. Sturm, A. Robert, P. Dechambenoit, F. Röhricht, R. Herges, H. Bock, F. Durola, *Chem. Sci.* **2018**, *9*, 8930–8936.

[22] A. Narita, X.-Y. Wang, X. Feng, K. Mullen, *Chem. Soc. Rev.* **2015**, *44*, 6616–6643.

[23] A. Shiotari, I. Hamada, T. Nakae, S. Mori, T. Okujima, H. Uno, H. Sakaguchi, Y. Hamamoto, Y. Morikawa, Y. Sugimoto, *Nano Lett.* **2020**, *20*, 8339–8345.

[24] X.-Y. Wang, X. Yao, K. Müllen, *Sci. China Chem.* **2019**, *62*, 1099–1144.

[25] J. Ma, K. Zhang, K. S. Schellhammer, Y. Fu, H. Komber, C. Xu, A. A. Popov, F. Hennersdorf, J. J. Weigand, S. Zhou, W. Pisula, F. Ortmann, R. Berger, J. Liu, X. Feng, *Chem. Sci.* **2019**, *10*, 4025–4031.

[26] R. G. Lawton, W. E. Barth, *J. Am. Chem. Soc.* **1971**, *93*, 1730–1745.

[27] K. Yamamoto, T. Harada, M. Nakazaki, T. Naka, Y. Kai, S. Harada, N. Kasai, *J. Am. Chem. Soc.* **1983**, *105*, 7171–7172.

[28] S. H. Pun, Q. Miao, *Acc. Chem. Res.* **2018**, *51*, 1630–1642.

[29] K. Kawasumi, Q. Zhang, Y. Segawa, L. T. Scott, K. Itami, *Nat. Chem.* **2013**, *5*, 739–744.

[30] L. T. Scott, M. M. Hashemi, M. S. Bratcher, *J. Am. Chem. Soc.* **1992**, *114*, 1920–1921.

[31] P. U. Biedermann, S. Pogodin, I. Agranat, *J. Org. Chem.* **1999**, *64*, 3655–3662.

[32] V. E. Clar, *The Aromatic Sextet*, John Wiley & Sons Ltd, New York, **1972**.

[33] M. Solà, *Front. Chem.* **2013**, *1*, 1.

[34] D. W. Szczepanik, M. Andrzejak, J. Dominikowska, B. Pawełek, T. M. Krygowski, H. Szatylowicz, M. Solà, *Phys. Chem. Chem. Phys.* **2017**, *19*, 28970–28981.

[35] D. W. Szczepanik, M. Andrzejak, K. Dyduch, E. Żak, M. Makowski, G. Mazur, J. Mrozek, *Phys. Chem. Chem. Phys.* **2014**, *16*, 20514–20523.

[36] J. Jusélius, D. Sundholm, J. Gauss, *J. Chem. Phys.* **2004**, *121*, 3952–3963.

[37] H. Fliegl, S. Taubert, O. Lehtonen, D. Sundholm, *Phys. Chem. Chem. Phys.* **2011**, *13*, 20500–20518.

[38] D. Sundholm, H. Fliegl, R. J. F. Berger, *Wiley Interdiscip. Rev. Comput. Mol. Sci.* **2016**, *6*, 639–678.

[39] M. Buhl, M. Kaupp, V. G. Malkin, M. Bühl, *Calculation of NMR and EPR Parameters*, Wiley-VCH, Weinheim, FRG, **2004**.

[40] R. Islas, T. Heine, G. Merino, *Acc. Chem. Res.* **2012**, *45*, 215–228.

[41] W. E. Barth, R. G. Lawton, *J. Am. Chem. Soc.* **1966**, *88*, 380–381.

[42] T. J. Seiders, K. K. Baldridge, E. L. Elliott, G. H. Grube, J. S. Siegel, *J. Am. Chem. Soc.* **1999**, *121*, 7439–7440.

[43] A. M. Orendt, J. C. Facelli, S. Bai, A. Rai, M. Gossett, L. T. Scott, J. Boerio-Goates, R. J. Pugmire, D. M. Grant, *J. Phys. Chem. A* **2000**, *104*, 149–155.

[44] P. R. von Schleyer, H. Jiao, *Pure Appl. Chem.* **1996**, *68*, 209–218.

[45] G. Merino, T. Heine, G. Seifert, *Chem. Eur. J.* **2004**, *10*, 4367–4371.

[46] A. G. G. Papadopoulos, N. D. D. Charistos, A. Muñoz-Castro, *ChemPhysChem* **2017**, *18*, 1499–1502.

[47] P. Lazzeretti, *Prog. Nucl. Magn. Reson. Spectrosc.* **2000**, *36*, 1–88.

[48] R. Benassi, P. Lazzeretti, F. Taddei, *J. Phys. Chem.* **1975**, *79*, 848–851.

[49] J. Kruszewski, T. M. Krygowski, *Tetrahedron Lett.* **1972**, *13*, 3839–3842.

[50] P. Bultinck, R. Ponec, S. Van Damme, *J. Phys. Org. Chem.* **2005**, *18*, 706–718.

[51] E. Matito, *Phys. Chem. Chem. Phys.* **2016**, *18*, 11839–11846.

[52] E. Matito, M. Duran, M. Solà, *J. Chem. Phys.* **2005**, *122*, 014109.

[53] E. Matito, M. Duran, M. Solà, *J. Chem. Phys.* **2006**, *125*, 059901.

[54] D. W. Szczepanik, E. Żak, K. Dyduch, J. Mrozek, *Chem. Phys. Lett.* **2014**, *593*, 154–159.

[55] D. W. Szczepanik, *Comput. Theor. Chem.* **2016**, *1080*, 33–37.

[56] Z. Badri, C. Foroutan-Nejad, *Phys. Chem. Chem. Phys.* **2016**, *18*, 11693–11699.
[57] L. Zhao, R. Grande-Aztatzi, C. Foroutan-Nejad, J. M. Ugalde, G. Frenking, *ChemistrySelect* **2017**, *2*, 863–870.
[58] J. Poater, I. García-Cruz, F. Illas, M. Solà, *Phys. Chem. Chem. Phys.* **2004**, *6*, 314–318.
[59] M. Solà, *Wiley Interdiscip. Rev. Comput. Mol. Sci.* **2019**, *9*, e1404.